Observation of a giant band splitting in altermagnetic MnTe

T. Osumi [1], S. Souma [2,3,*], T. Aoyama,[1] K. Yamauchi [4], A. Honma,[1] K. Nakayama [1],
T. Takahashi,[1] K. Ohgushi,[1] and T. Sato[1,2,3,5,6,†]

[1]*Department of Physics, Graduate School of Science, Tohoku University, Sendai 980-8578, Japan*
[2]*Center for Science and Innovation in Spintronics, Tohoku University, Sendai 980-8577, Japan*
[3]*Advanced Institute for Materials Research (WPI-AIMR), Tohoku University, Sendai 980-8577, Japan*
[4]*Center for Spintronics Research Network, Osaka University, Toyonaka, Osaka 560-8531, Japan*
[5]*International Center for Synchrotron Radiation Innovation Smart, Tohoku University, Sendai 980-8577, Japan*
[6]*Mathematical Science Center for Co-creative Society, Tohoku University, Sendai 980-8577, Japan*

We performed angle-resolved photoemission spectroscopy (ARPES) on hexagonal MnTe, a candidate for an altermagnet with a high critical temperature ($T_N = 307$ K). By utilizing photon-energy-tunable ARPES in combination with first-principles calculations, we found that the band structure in the antiferromagnetic phase exhibits a strongly anisotropic band-splitting associated with the time-reversal-symmetry breaking, providing direct experimental evidence for the altermagnetic band splitting. The magnitude of the splitting reaches 0.8 eV at non-high-symmetry momentum points, which is much larger than the spin-orbit gap of $\sim$0.3 eV along the ΓK high-symmetry cut. The present result paves the way toward realizing exotic physical properties associated with the altermagnetic spin splitting.

I. INTRODUCTION

A new type of magnetism called "altermagnetism" is attracting a great deal of attention because it is regarded as a third type of magnetism not categorized as conventional ferromagnetism or antiferromagnetism [1,2]. In ferromagnets, the energy bands are spin split due to the breaking of time-reversal symmetry (TRS). In colinear antiferromagnets, the energy bands are generally spin degenerate because of the antiparallel configuration of the magnetic moment and the zero net magnetization. Intriguingly, altermagnets are different from these two magnets; despite the zero magnetization as in antiferromagnets, the bands in altermagnets are spin split due to the TRS breaking as in ferromagnets. This band splitting is guaranteed by the existence of opposite-spin sublattices connected by the crystal-rotation symmetries [1–5]. In contrast to ferromagnets, in which the band splitting is typically isotropic in the momentum (k) space, altermagnets exhibit anisotropic band splitting. This is because the sign of the band splitting must be reversed between the positive and negative k's to meet the requirement from the zero net magnetization, leading to band splitting with nodes on high-symmetry lines in the bulk Brillouin zone (BZ) in the absence of spin-orbit coupling (SOC). Although anisotropic band splitting appears in nonmagnets as a consequence of space-inversion-symmetry breaking and SOC [6], the altermagnetic band splitting is distinct from it because the splitting appears even without SOC [1–5,7,8]. Besides the fundamental interest in unconventional band splitting, the altermagnetic band splitting is predicted

to host a variety of exotic quantum phenomena such as the anomalous Hall effect, spin current generation, spin splitter torque, magnetic circular dichroism, the crystal Nernst effect, and the piezomagnetic effect [1,2,5,9–17]. Some of them were recently verified experimentally [18–26]. However, direct experimental evidence of altermagnetic band splitting, which would serve as a basis to understand the exotic phenomena of altermagnets, is still missing. Such a lifting of spin degeneracy in the energy bands would be unexpected for conventional antiferromagnets and, indeed, has not been observed to date. Experimentally verifying the altermagnetic band splitting to establish this new class of magnet and further advance the exciting physics of unconventional magnets is thus urgently required.

Here we focus on hexagonal MnTe, which is suitable for observing the possible large spin splitting [1,15,16] due to its high Néel temperature ($T_N = 307$ K) [27–30]. MnTe crystallizes in the NiAs-type structure (space group: $P6_3/mmc$) consisting of alternately stacked Mn and Te planes characterized by a simple hexagonal Mn lattice and a hexagonal close-packed Te lattice with AB stacking [for crystal structure and the bulk BZ, see Figs. 1(a) and 1(b), respectively] [31]. In the antiferromagnetic (AFM) phase, the Mn^{2+} ions placed at the center of the Te octahedra are ferromagnetically aligned within the same Mn plane with the magnetic moment lying in the (0001) plane, whereas the Mn ions between adjacent Mn planes are antiferromagnetically coupled [28,29,32]. Intriguingly, opposite-spin sublattices essential for altermagnetism are realized in the Mn sites because the octahedral coordination is inequivalent between the AB- and BA-stacked Mn sites. This situation does not allow spin reversal with a single symmetry operation and leads to the breaking of global TRS. The density-functional-theory (DFT) calculations predict a

*Corresponding author: s.souma@arpes.phys.tohoku.ac.jp
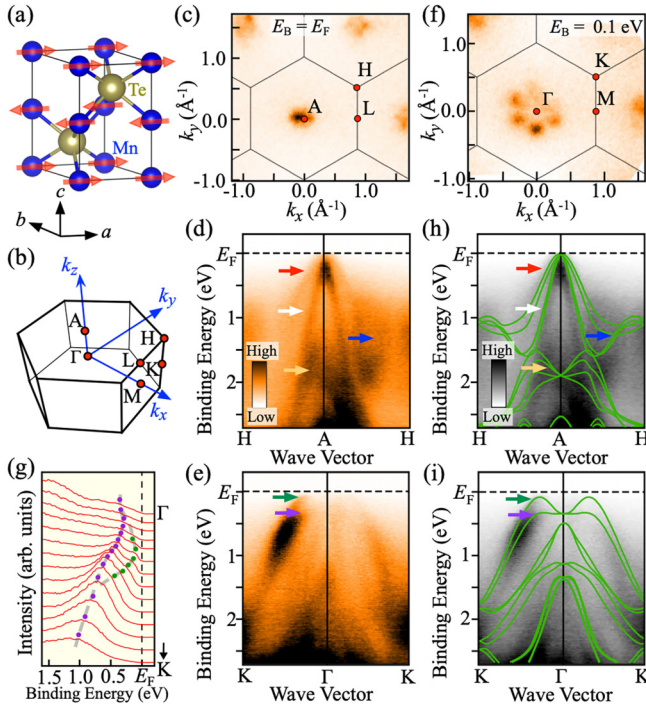†Corresponding author: t-sato@arpes.phys.tohoku.ac.jp

FIG. 1. (a) Crystal structure and (b) bulk hexagonal BZ of MnTe. Ther spin configuration for the $S_{a\parallel}$ case is indicated by red arrows in (a). (c) ARPES intensity maps at $T = 40$ K as a function of k_x and k_y at $E_B = E_F$ for the $k_z \sim \pi$ (*AHL*) plane. ARPES intensity as a function of the wave vector and E_B measured along (d) the *AH* cut of the bulk BZ obtained at $h\nu = 117$ eV and (e) the ΓK cut at $h\nu = 80$ eV. (f) Same as (c), but at $E_B = 0.1$ eV for the $k_z \sim 0$ (ΓKM) plane. (g) EDCs near E_F along the ΓK cut. Calculated band structures along the (h) *AH* and (i) ΓK cuts for the AFM phase with the ($S_{a\parallel}$, ΓK_2) configuration while including the spin-orbit coupling (SOC), overlaid with the ARPES intensity in gray scale.

giant spin splitting [1,15,16,33], although such a splitting has yet to be clarified.

In this article, we report an angle-resolved photoemission spectroscopy (ARPES) study of a MnTe bulk single crystal and show direct evidence of the altermagnetic band splitting. This was enabled by the utilization of photon-energy-tunable microfocused ARPES in combination with DFT calculations. We find that the magnitude of altermagnetic band splitting strongly depends on the k location in the three-dimensional (3D) BZ and is also affected by the SOC. We discuss the implications of the present results in relation to other experiments on altermagnets.

II. EXPERIMENTS

Single crystals of MnTe were grown using the chemical vapor transport method with I_2 as the agent gas. Obtained single crystals were characterized by x-ray diffraction, magnetization, and electrical resistivity measurements. Details of the sample preparation and characterization were described elsewhere [25] (see also Appendix A). ARPES measurements were performed with microfocused vacuum-ultraviolet (VUV) synchrotron light at BL-28A in photon factory (PF) [34]. We used linearly polarized light of 60–170 eV. The

energy resolution was set to be 10–20 meV. Samples were cleaved *in situ* along the (0001) plane of the hexagonal crystal in an ultrahigh vacuum of 1×10^{-10} Torr. The crystal orientation was determined by an x-ray Laue backscattering measurement consistent with the (0001) cleaved plane. Since MnTe single crystal is hard to cleave, we tried to cleave several times in an ultrahigh vacuum and occasionally obtained a small, flat area of the crystal a few tens of microns square and then focused the micro photon beam on it. Temperature during ARPES measurements was set at $T = 30$–310 K, which covers T_N (= 307 K). The Fermi level E_F of the samples was referenced to that of a gold film electrically in contact with the sample holder. First-principles band-structure calculations were carried out by using a projector augmented wave method implemented in the Vienna *Ab initio* Simulation Package (VASP) code [35] with the generalized gradient approximation pseudopotential. The lattice constants were fixed to the experimental values ($a = b = 4.158$ Å and $c = 6.726$ Å) [36]. The total energy was calculated self-consistently with tetrahedron sampling of a $12 \times 12 \times 8$ k-point mesh taking into account SOC.

III. RESULTS AND DISCUSSION

First, we discuss the overall band structure of MnTe in the AFM phase. We carried out $h\nu$-dependent ARPES measurements and estimated the k_z value (see Fig. 6 in Appendix B). The contour map of ARPES intensity at E_F for the *AHL* plane obtained with $h\nu = 117$ eV in Fig. 1(c) signifies a bright spot centered at each A point that follows the periodicity of the hexagonal BZ. The band dispersion along the *AH* high-symmetry cut shown in Fig. 1(d) signifies a dispersive hole band (white arrow) at the A point, together with a shallower hole band outside this band (red arrow). These bands produce a spot centered at the A point in Fig. 1(c). One can also recognize in Fig. 1(d) a broad feature at the binding energy E_B of ~ 2 eV around the A point (yellow arrow) and another broad feature which weakly disperses upward on approaching the H point (blue arrow). We carried out the ARPES measurements also for the ΓKM plane with $h\nu = 80$ eV and found that the band dispersion [Fig. 1(e)] and the energy contour [Fig. 1(f)] are markedly different. As shown in Fig. 1(e), instead of a simple hole band, the top of the valence band along the ΓK cut shows an M-shaped dispersion with its maxima slightly away from the Γ point (green arrow), producing six petals surrounding the Γ point in Fig. 1(f).

To discuss the band character in more detail, we show in Fig. 1(g) the energy distribution curves (EDCs) around E_F along the ΓK cut. The result signifies band splitting with a maximum value of ~ 0.3 eV slightly away from the Γ point. This band splitting is also seen in Fig. 1(e) (green and purple arrows) and associated with SOC. We found that the DFT calculations with a spin configuration and experimental geometry of either the ($S_{a\parallel}$, ΓK_2) or ($S_{a\perp}$, ΓK_1) setting reproduce well the experimental results (for details, see Appendix C). Since these two cases show almost identical band structures, we hereafter adopt the former case just for our convenience.

As shown in Fig. 1(h), the experimental band structure along the *AH* cut is well reproduced by the band calculation. In particular, the steeper inner hole band (white arrow) and
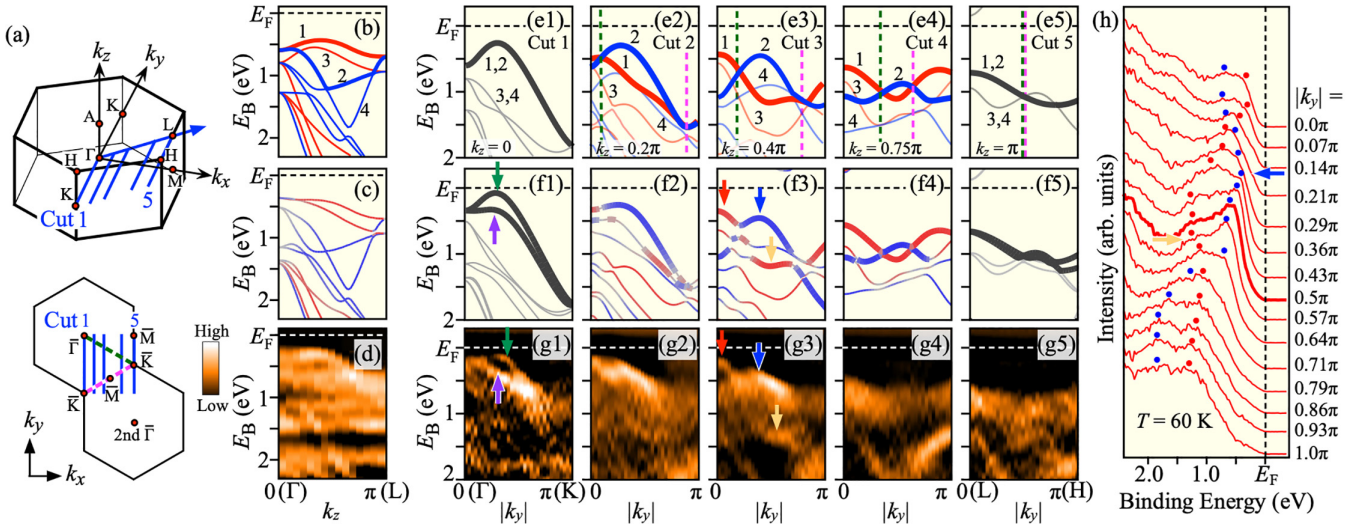
FIG. 2. (a) Bulk BZ (top) and surface BZ (bottom) of MnTe, together with the k cuts (blue solid lines) where calculations and ARPES measurements shown in (e)–(g) were carried out. Calculated band structure along the ΓL cut in the AFM phase (b) without and (c) with SOC. Red and blue curves correspond to up and down spin components, respectively, in which the quantization axis for spins is defined along the k_y axis. Gray corresponds to zero spin polarization. (d) Second-derivative plot of ARPES intensity at $T = 40$ K along the ΓL cut. Calculated band structures in the AFM phase (e) without and (f) with SOC along the k_y cut passing through the ΓL line (cuts 1–5) shown by blue lines in (a). Thick red and blue curves highlight bands 1 and 2, respectively. Calculations for cuts 1–5 were carried out at $(k_x, k_z) = (0, 0)$, $(0.2\pi, 0.2\pi)$, $(0.4\pi, 0.4\pi)$, $(0.75\pi, 0.75\pi)$, and (π, π), respectively. $|k_y| = \pi$ corresponds to the ΓK length. Green and purple dashed lines correspond to the k point on the $\overline{\Gamma K}$ high-symmetry line of the surface BZ, as also indicated in the bottom panel in (a). (g) Corresponding second-derivative plots of ARPES intensity as a function of $|k_y|$ measured along cuts 1–5. (h) EDCs corresponding to the band mapping of (g3) at $T = 60$ K. Red and blue dots trace bands 1 and 2, respectively. Yellow and blue arrows shown in (g3) are also plotted.

the outer hole band (red arrow), as well as the feature at $E_B \sim 1.3$–2.0 eV (yellow and blue arrows) seen by ARPES, are well reproduced by the calculation. These bands are attributed to the hybridized Te $5p$ and Mn $3d$ t_{2g} orbitals. We also found overall agreement of the band dispersions between the experiment and calculation along the ΓK cut [Fig. 1(i)]. The valence-band top is experimentally located at the A point around E_F, in line with the calculation, signifying the semiconducting nature of MnTe. Taking into account the total band-gap size of ~ 1.3 eV [37,38], it is suggested that MnTe is a p-type semiconductor, consistent with the transport measurement [39,40].

Next, we focus on the observation of the altermagnetic band splitting. Since the altermagnetic band splitting was predicted to have nodes along high-symmetry lines under negligible SOC, it is necessary to carry out ARPES measurements along non-high-symmetry cuts to observe the altermagnetic band splitting. The non-high-symmetry ΓL cut [see Fig. 2(a)] is suited to this task because the DFT calculations identified a sizable splitting along this cut [1,15]. On the other hand, the ARPES measurement needs special care because $h\nu$ must be changed at every step of momentum to correctly sweep $\mathbf{k}$ along the ΓL cut. Since the altermagnetic band splitting can show up even without SOC, we first explain the calculated band structure without SOC shown in Fig. 2(b). One can recognize the spin-split bands in a whole $(E, \mathbf{k})$ region. Although many bands are observed in this region, one can easily identify the spin-split partner of each band, thanks to the band degeneracy along high-symmetry lines. For example, bands labeled 1 and 2 (sequentially labeled from the high-

est occupied band around Γ) are spin-split partners to each other because they degenerate at the Γ and L points. The altermagnetic band-splitting associated with these bands is strongly anisotropic; it reaches ~ 0.8 eV at around $k_z \sim 0.5\pi$, whereas it is zero at the Γ ($k_z = 0$) and L ($k_z = \pi$) points. Similarly, the altermagnetic band splitting for bands 3 and 4 has nodes at the Γ and L points and takes a maximum at ~ 1.0 eV around $k_z \sim 0.7\pi$. Band 2 intersects band 3 due to the large spin splitting. Such large splitting is associated with the $\mathcal{PT}$ (space- and time-reversal) symmetry breaking of the Te site and strong hybridization between Te $5p$ and Mn $3d$ orbitals. When the SOC is included in the calculation, these bands hybridize each other to produce a small spin-orbit gap at the intersection, but the overall spin-splitting feature is essentially preserved [Fig. 2(c)]. Although the inclusion of SOC makes the assignment of spin-spilt partners not very straightforward, one can discuss the characteristics of the spin splitting by referring to the calculations without SOC. As shown in Fig. 2(d), the experimental band structure along the ΓL cut shows rough agreement with the calculation [Figs. 2(b) or 2(c)].

To investigate the altermagnetic band splitting in more detail, we performed ARPES measurements along representative $\mathbf{k}$ cuts which cross the $\mathbf{k}$ points in the ΓKHL plane, including the ΓL cut [cuts 1–5 in Fig. 2(a)]. Cut 1 with $(k_x, k_z) = (0, 0)$ and cut 5 with $(k_x, k_z) = (\pi, \pi)$ correspond to the ΓK and LH high-symmetry cuts, respectively, whereas cuts 2–4 trace non-high-symmetry $\mathbf{k}$ points. Figures 2(g), 2(e), and 2(f) show the obtained ARPES intensity, the corresponding calculated band structures without SOC, and those with

SOC, respectively. The calculated bands along the ΓK cut (cut 1) in Fig. 2(e1) are spin degenerate irrespective of $\mathbf{k}$ when the SOC is neglected, as highlighted by the case of bands 1 and 2 (thick black curves). When the SOC is included, the degeneracy is lifted in most of the $\mathbf{k}$ points except for the Γ point. The spin polarization remains zero along the entire ΓK line due to the twofold rotation and mirror symmetries of the crystal [Fig. 2(f1)]. As the $\mathbf{k}$ cut moves away from the high-symmetry $\mathbf{k}$ points, the bands start to spin split [cut 2; Fig. 2(e2)]. In particular, bands 1 and 2, indicated by thick red and blue curves, respectively, show a strongly $\mathbf{k}$-dependent exchange splitting accompanied by the sign reversal upon varying k_y, in contrast to the case of a simple itinerant ferromagnet showing a $\mathbf{k}$-independent exchange splitting. We found that the $\mathbf{k}$ points at which the sign reversal occurs are exactly on the $\overline{\Gamma K}$ high-symmetry lines of the surface BZ. A similar anisotropic band splitting is also recognized along cuts 3 and 4 [Figs. 2(e3) and 2(e4)], whereas the overall magnitude is gradually suppressed and eventually vanishes along the high-symmetry LH cut [cut 5; Fig. 2(e5)]. Intriguingly, the magnitude of calculated altermagnetic band splitting reaches $+0.8$ eV at $|k_y| \sim 0.25\pi$ and -0.8 eV at $|k_y| \sim 0.5\pi$ along cut 3 (we define positive splitting when the energy level of band 1 is higher than that of band 2 and vice versa for the negative splitting).

The experimental band structure [Fig. 2(g)] shows reasonable agreement with the calculated band dispersion including SOC [Fig. 2(f)]. For example, one can recognize a common trend in which the topmost band gradually sinks downward and becomes flatter on moving from cut 1 to cut 5 in both the experiment and calculation. Along cut 1 (the ΓK cut), the SOC-induced band splitting of the topmost valence band (green and purple arrows) is reproduced by the calculation, as already shown in Fig. 1. Along cut 3, the calculation signifies two local maxima in the band dispersion at the Γ point for band 1 (red arrow) and slightly away from the Γ point for band 2 ($|k_y| \sim 0.4\pi$; blue arrow). Since these bands are the spin-split partners, the experimental observation of a double-peaked dispersion along cut 3 supports the existence of altermagnetic band splitting. We also find a signature of the band bottom (yellow arrow) which may correspond to the local minimum of calculated band 1. To trace the energy dispersion of split bands in a more straightforward way, we show in Fig. 2(h) a series of EDCs obtained along cut 3. One can recognize peaks corresponding to band 1 (red dots) and band 2 (blue dots) which seem to intersect at specific k_y positions (e.g., at $|k_y| \sim 0.21\pi$ and 0.71π), consistent with the calculated band structure shown in Fig. 2(e3) (strictly speaking, these bands do not intersect due to the spin-orbit gap, although the gap is experimentally unclear, probably due to the lifetime broadening and/or k_z broadening). Importantly, at $|k_y| = 0.43\pi$, bands 1 and 2 are located at binding energies of 1.25 and 0.45 eV, respectively, corresponding to altermagnetic band splitting of ~ 0.8 eV, which has a magnitude comparable to that of the calculation. Moreover, one can see that both the general trend of band dispersion and the overall energy position of bands 1 and 2 are similar between the experiment and calculation. In fact, the yellow and blue arrows indicated in the second-derivative plot in Fig. 2(g3) well coincide with the peak positions of the EDCs for bands 1 and 2 in
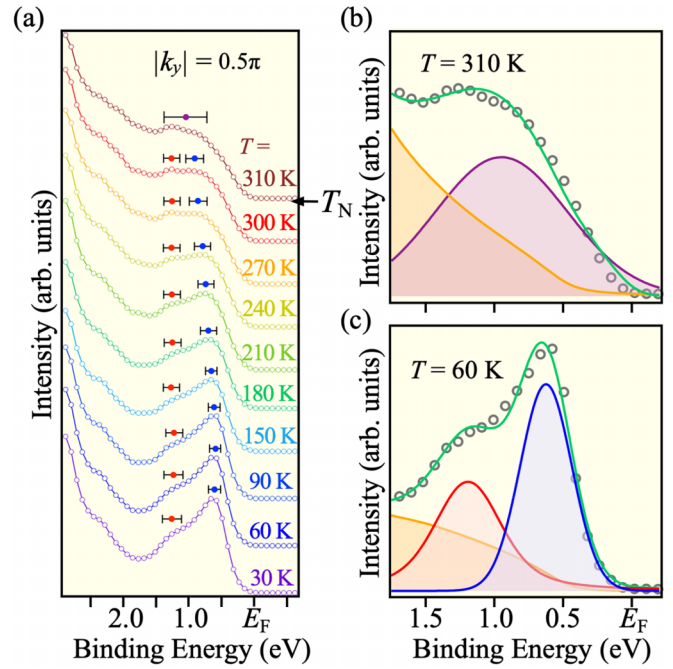

FIG. 3. (a) Temperature dependence of EDC at $|k_y| = 0.5\pi$ shown by the thick curve in Fig. 2(h). Red and blue dots show the energy positions of peaks estimated by numeric simulations of EDCs assuming Voigt-function peak(s) and moderate background. Results of numerical simulations at (b) $T = 310$ K (above T_N) and (c) 60 K (below T_N).

Fig. 2(h). These support our assignment of the experimental band dispersion, namely, the altermagnetic band splitting between these bands. We find that the overall agreement between the experiment and calculation becomes rather poor along cut 4. This is likely due to the smaller band splitting that causes difficulty in experimentally distinguishing bands 1 and 2, consistent with the general trend that the calculated band splitting takes the largest value at $k_z \sim 0.4\pi$ (cut 3). It is noted that the bright feature at $E_B = 1.3$–2.0 eV in Fig. 2(g4) is likely associated with band 3, while the energy position is slightly lower than the calculation, probably due to the k_z broadening effect in the experiment and/or overestimation of the band energy in the calculation. It is also remarked that the band width in the experiment in Figs. 2(g1)–2(g5) appears to be slightly different from that in the calculation in Figs. 2(f1)–2(f5), as inferred from the narrower band width in the experiment along cut 1 [compare the energy positions of bands at the K point between Figs. 2(f1) and 2(g1)]. This difference may be associated with the electron correlation effect, which is not taken into account in the calculation.

To further validate the altermagnetic origin of the observed band splitting, we performed temperature-dependent ARPES measurements at $|k_y| = 0.5\pi$ along cut 3, where the altermagnetic band splitting is clearly observed [highlighted by the thick EDC in Fig. 2(h)]. As shown in Fig. 3(a), at $T = 30$ K, one can recognize two peaks at $E_B = 1.2$ and 0.6 eV due to the altermagnetic band splitting. On increasing temperature, two peaks gradually merge and eventually become indistinguishable at $T \sim 300$–310 K. This systematic evolution can hardly be explained in terms of a simple change in the spec-
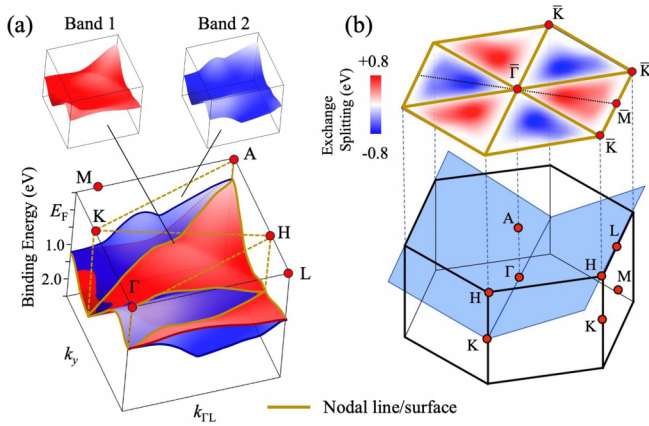
FIG. 4. (a) Schematic 3D band dispersion of MnTe in the ΓKHL plane without SOC, signifying the dispersive Dirac-nodal lines running along the $\overline{\Gamma KM}$ high-symmetry lines of the surface BZ (orange curves). (b) ΓKHL plane (shaded area) in the 3D BZ in which the band dispersion in (a) is shown. The intensity plot of the calculated altermagnetic band splitting in the hexagonal surface BZ is shown in the top panel.

tral weight, as suggested by our numerical simulation (for details, see Appendix D). The temperature at which the two peaks merge coincides with T_N, suggesting that the splitting is associated with the AFM transition. Such a change in the band splitting is also supported by numerical simulations of the EDC at each temperature that take into account the single or double Voigt-function peaks and moderate background, as highlighted in Figs. 3(b) and 3(c), where the EDCs at $T = 310$ K (above T_N) and 60 K (well below T_N) are reasonably reproduced by the single and double peaks, respectively. All these results provide spectroscopic evidence of the existence of altermagnetic band splitting in the colinear AFM phase of MnTe. The next challenge is to accurately determine the **k**-dependent spin texture by spin-resolved micro-ARPES measurement.

To highlight our key findings, we draw in Fig. 4(a) the schematic band dispersion for the spin-split partners, bands 1 and 2, in the ΓKHL plane based on the DFT calculation supported by the ARPES observation. When the SOC is neglected, these bands are degenerate along the ΓK and LH high-symmetry lines, producing dispersive nodal lines (orange curves) across which the sign of altermagnetic band splitting is reversed. Additional nodal lines running along the $\overline{\Gamma K}$ cut exist. All these nodal lines are regarded as a slice of nodal surfaces in the ΓKHA and MKHL planes. The existence of multiple nodal lines is also visualized by the intensity plot of calculated altermagnetic band splitting in the hexagonal BZ in Fig. 4(b), where one can recognize the nodal lines running along the $\overline{\Gamma K}$ and $\overline{KM}$ high-symmetry lines of the surface BZ as well as the sign reversal of altermagnetic band splitting across the nodal lines. Such sign-reversal band splitting is a unique characteristic of altermagnets, distinct from conventional sign-preserving ferromagnetic exchange splitting.

When the SOC is included, the band degeneracy of the nodal surfaces is lifted by the spin-orbit gap in the entire BZ, whereas the bands are still spin degenerate along some partic-

ular high-symmetry lines such as the ΓA line, protected by the C_{2z} symmetry of the crystal. Low-energy excitations of such nodal lines are characterized by the altermagnetic quasiparticle with a quadratic band dispersion [1]. Importantly, since the overall energy scale of the spin-orbit gap (<0.3 eV) is smaller than that of the altermagnetic band splitting (<0.8 eV), the anisotropic sign-reversal exchange splitting, a key characteristic of altermagnets, is still maintained even in the presence of SOC. The present result thus establishes that the theoretically predicted altermagnetic band splitting is, indeed, realized in MnTe. It is emphasized that the altermagnetic band splitting verified in this study is responsible for the piezomagnetic effect and the x-ray magnetic circular dichroism recently reported for MnTe [24,25], both of which are sensitive to the global TRS breaking. Also, the multiple band crossings and sign reversal of the altermagnetic band splitting inherent in MnTe would give rise to a high Berry curvature region in **k** space and may be responsible for the spontaneous anomalous Hall effect, as experimentally verified recently [22].

The micro-ARPES measurements and the DFT calculations have established the presence of altermagnetic band splitting in the colinear AFM phase of MnTe. The altermagnetic band splitting is strongly **k** dependent and reaches ~ 0.8 eV at non-high-symmetry **k** points in the ΓKHL plane, whereas the splitting at the high-symmetry **k** points is suppressed, producing multiple nodal lines. We also observed a small (~ 0.3 eV) band splitting along the high-symmetry ΓK cut, suggesting an additional contribution from the SOC. The present results lay the foundation for exploring unique physical properties inherent in the altermagnetic MnTe, paving a path toward investigating the altermagnetic band splitting in other altermagnets.

APPENDIX A: SAMPLE CHARACTERIZATION

We show in Fig. 5(a) a photograph of a typical single crystal used in this study. The details of the sample preparation and characterization were described elsewhere [25]. Orientation of the crystal and good single crystallinity were confirmed by the x-ray Laue backscattering measurement which shows clear sixfold symmetric diffraction spots, as seen in Fig. 5(b). The clean surface nature of the crystal cleaved in ultrahigh vacuum of 1×10^{-10} Torr was confirmed by sharp core-level peaks originating from the Mn $3p$ and Te $4d$ orbitals with no inclusion of contaminant peaks, as shown in Fig. 5(c).
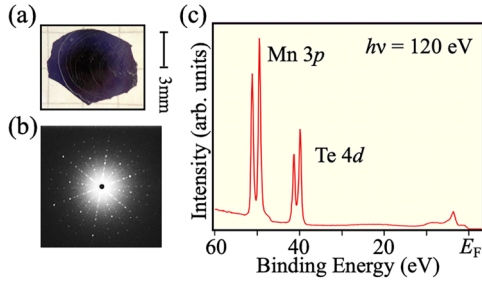
FIG. 5. (a) Photograph of a MnTe single crystal. (b) Representative Laue x-ray diffraction pattern of the (0001) surface. (c) Photoemission spectrum of MnTe in a wide energy region obtained at $h\nu = 120$ eV.

APPENDIX B: NORMAL-EMISSION ARPES SPECTRA

Figures 6(a) and 6(b) show the EDCs and corresponding ARPES intensity, respectively, along the wave vector perpendicular to the sample surface k_z, measured with the normal-emission setup by varying $h\nu$ in the VUV region ($h\nu = 60$–170 eV). One can find some energy bands displaying finite k_z dispersion, e.g., in an E_B range of E_F–0.7 and 1.2–2.6 eV. The observed band dispersions well follow the periodicity of the bulk Brillouin zone as well as the calculated band dispersion including SOC (green curves). The periodic dispersion along the k_z direction indicates the bulk origin of the observed bands.

APPENDIX C: BAND-STRUCTURE CALCULATIONS WITH DIFFERENT IN-PLANE SPIN CONFIGURATIONS

In the presence of SOC, the energy eigenvalue in the AFM phase generally differs depending on the spin direction [33]. Although the magnetic torque and neutron diffraction exper-

iments [28,29,32] have suggested an in-plane nature of the magnetic moment in the AFM phase, it is experimentally unclear whether the magnetic moment is directed along the *a* axis corresponding to the nearest neighbor Mn-Mn bonding direction (k_y axis in k space) or perpendicular to it (k_x axis in k space). To examine to what extent the choice of possible spin configurations and the selection of inequivalent **k** cuts influence the calculated band structure, we carried out DFT calculations for bulk MnTe with spin configurations parallel and perpendicular to the *a* axis, denoted here $S_{a\parallel}$ and $S_{a\perp}$, respectively. Here we focus on the band dispersion along the ΓK cuts because the band splitting of the topmost valence band is useful to pin down a possible spin configuration and actual **k** cuts in the experiment. For the $S_{a\parallel}$ configuration, two inequivalent ΓK cuts exist, one directed along the spin axis, ΓK_1, and the other rotated by 60° from it, ΓK_2 [Fig. 7(b)]. For the calculation with the $S_{a\perp}$ configuration, we fix these **k** cuts but just rotate the spin direction by 90°. As shown in Fig. 7(c) for the $S_{a\parallel}$ configuration, the band dispersion for the topmost valence band shows no band splitting along the ΓK_1 cut, whereas it apparently splits into two bands (bands 1 and 2) along the ΓK_2 cut [Fig. 7(d)] with a maximum splitting size of 0.25 eV. This difference is due to the symmetry difference of these two **k** cuts with respect to the magnetic moment. For the $S_{a\perp}$ configuration, the ΓK_1 cut exhibits a band splitting comparable to that of the ΓK_2 cut for the $S_{a\parallel}$ configuration, whereas the band splitting along the ΓK_2 cut is overall reduced. We show in Fig. 7(k) the experimental band dispersion determined by tracing the numerical fittings to the EDCs in Fig. 1(g), in comparison with the calculated band structure for four sets of possible spin configurations and **k** cuts. Taking into account that the experimental band splitting is as large as ~0.3 eV along the ΓK cut, it is likely that the experimental spin and measurement geometry is either ($S_{a\parallel}$, ΓK_2) or ($S_{a\perp}$, ΓK_1). As shown in Figs. 7(g)–7(j), there are
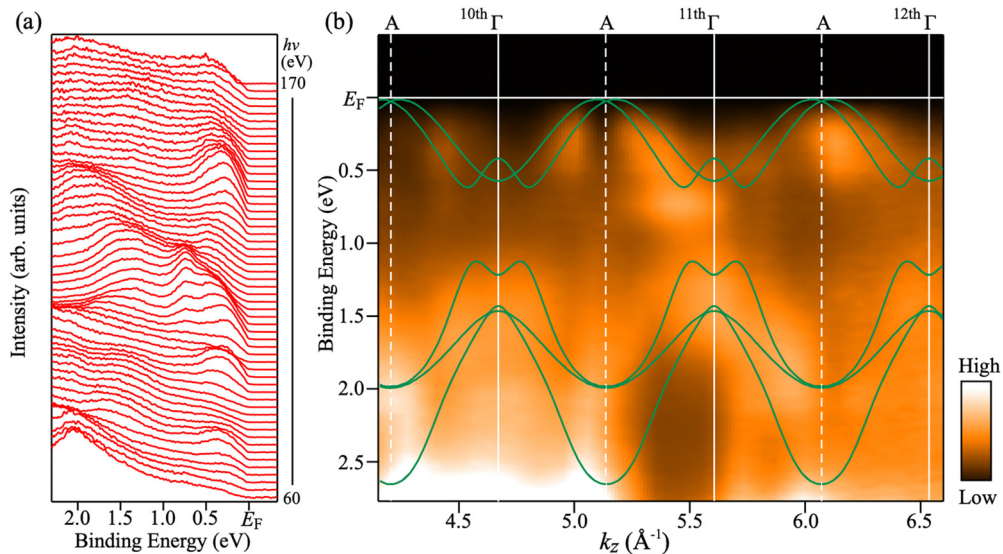

FIG. 6. Plots of (a) the normal-emission EDCs and (b) corresponding ARPES intensity as a function of $h\nu$ or k_z (corresponding to the out-of-plane ΓA cut). The inner potential was set to be $V_0 = 8.0$ eV from the periodicity of the band dispersion. Green curves represent the calculated band structure including SOC along the ΓA cut for the ($S_{a\parallel}$, ΓK_2) setting.
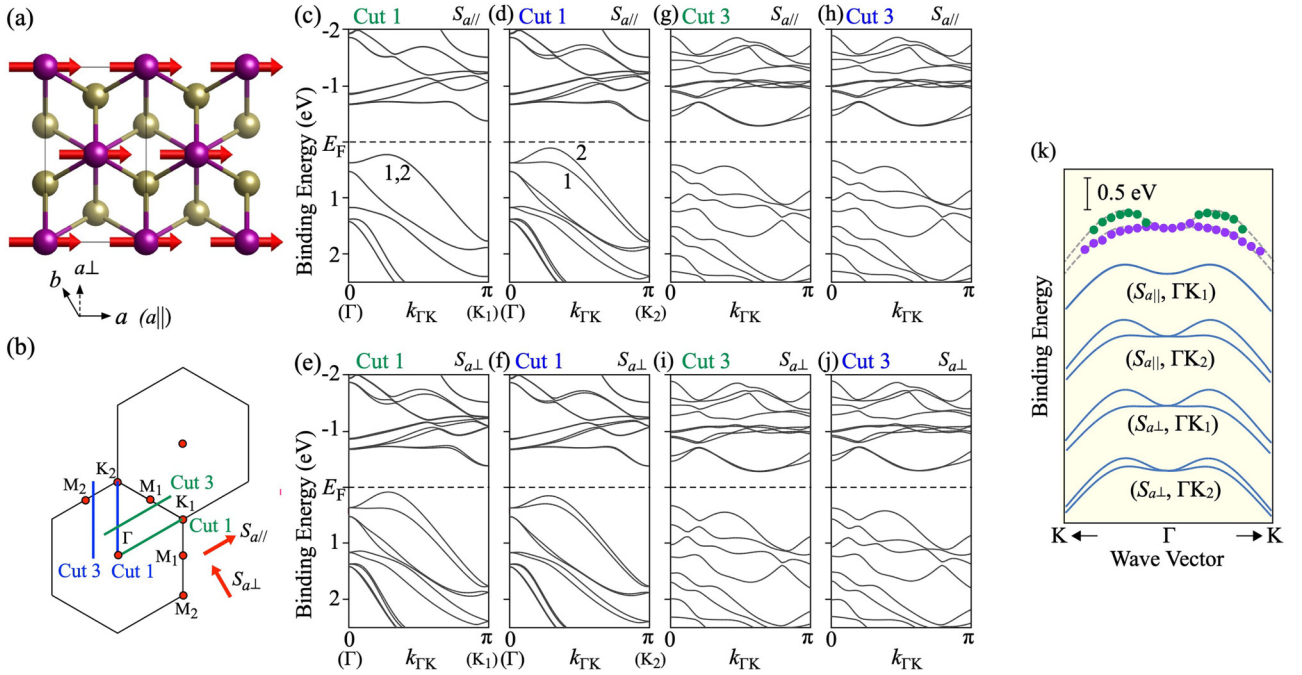
FIG. 7. (a) Crystal structure with the in-plane spin configuration, here called $S_{a\parallel}$. (b) k cuts in the surface BZ along which DFT calculations were carried out (green and blue lines). The direction of the spin vectors, $S_{a\parallel}$ and $S_{a\perp}$, is also indicated. We specify two inequivalent K points as K_1 and K_2 and the same for the M points (M_1 and M_2). As a result, the ΓK cut (cut 1; $k_z = 0$) has two configurations, namely, ΓK_1 and ΓK_2. Calculated band structure with SOC for the $S_{a\parallel}$ configuration along the (c) ΓK_1 and (d) ΓK_2 cuts. (e) and (f) Same as (c) and (d), but for the $S_{a\perp}$ configuration. (g)–(j) Same as (c)–(f), but for cut 3 ($k_z = 0.4\pi$). The definition of cuts 1 and 3 is the same as that in the main text. (k) Experimental band dispersion obtained by fitting to the EDCs in Fig. 1(g), compared with the calculated band structure along the ΓK cut in the AFM phase for the four sets of spin configurations.

not many differences in the band dispersion along cut 3. This suggests that the key band argument based on cut 3 in the main text is not very affected by the choice of **k** cuts and spin configurations.

APPENDIX D: TEMPERATURE-DEPENDENT ARPES SPECTRA

To examine in more detail the temperature-dependent change in the EDCs shown in Fig. 3(a), we show in Fig. 8(a) a plot of the EDCs with no vertical offset. One can see that energy position of the first peak located closer to E_F apparently moves toward higher binding energy upon increasing temperature. This systematic shift can hardly be explained in terms of the simple change in the spectral weight. To further examine this point, we performed numerical simulations of the EDC at $T = 310$ K by assuming two peaks with their energy positions fixed to those at $T = 30$ K. As a result, we found that it is difficult to reproduce the experimental EDC, no matter what broadening and spectral-weight parameters we use. This is highlighted by a simulation curve shown by the brown curve (best fit) in Fig. 8(b) in which one can recognize poorer agreement with the experimental EDC (open

circles) compared to the numerical simulation with a single peak [green curve; same as Fig. 3(b)]. These results suggest an intrinsic reduction of the exchange splitting with increasing temperature.
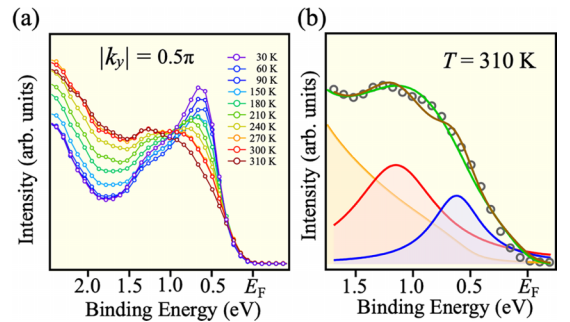

FIG. 8. (a) Same as Fig. 3(a), but without a vertical offset. (b) Result of the numerical simulation of the EDC at $T = 310$ K assuming two peaks with their peak positions fixed to those at $T = 30$ K (brown curve). The green curve represents the numerical simulation assuming a single peak [same as Fig. 3(b)].

[1] L. Šmejkal, J. Sinova, and T. Jungwirth, Phys. Rev. X **12**, 031042 (2022).

[2] L. Šmejkal, J. Sinova, and T. Jungwirth, Phys. Rev. X **12**, 040501 (2022).

[3] S. Hayami, Y. Yanagi, and H. Kusunose, J. Phys. Soc. Jpn. **88**, 123702 (2019).

[4] L.-D. Yuan, Z. Wang, J.-W. Luo, E. I. Rashba, and A. Zunger, Phys. Rev. B **102**, 014422 (2020).

[5] H.-Y. Ma, M. Hu, N. Li, J. Liu, W. Yao, J.-F. Jia, and J. Liu, Nat. Commun. **12**, 2846 (2021).

[6] E. I. Rashba, Sov. Phys. Solid State **2**, 1109 (1960).

[7] S. Hayami, Y. Yanagi, and H. Kusunose, Phys. Rev. B **102**, 144441 (2020).

[8] L. D. Yuan, Z. Wang, J. W. Luo, and A. Zunger, Phys. Rev. Mater. **5**, 014409 (2021).

[9] M. Naka, S. Hayami, H. Kusunose, Y. Yanagi, Y. Motome, and H. Seo, Nat. Commun. **10**, 4305 (2019).

[10] L. Šmejkal, R. González-Hernández, T. Jungwirth, and J. Sinova, Sci. Adv. **6**, eaaz8809 (2020).

[11] M. Naka, Y. Motome, and H. Seo, Phys. Rev. B **103**, 125114 (2021).

[12] I. I. Mazin, K. Koepernik, M. D. Johannes, R. González-Hernández, and L. Šmejkal, Proc. Natl. Acad. Sci. USA **118**, e2108924118 (2021).

[13] T. P. T. Nguyen and K. Yamauchi, Phys. Rev. B **107**, 155126 (2023).

[14] D. F. Shao, Y. Y. Jiang, J. Ding, S. H. Zhang, Z. A. Wang, R. C. Xiao, G. Gurung, W. J. Lu, Y. P. Sun, and E. Y. Tsymbal, Phys. Rev. Lett. **130**, 216702 (2023).

[15] S. Rooj, J. Chakraborty, and N. Ganguli, Adv. Phys. Res. **3**, 2300050 (2024).

[16] I. I. Mazin, Phys. Rev. B **107**, L100418 (2023).

[17] X. Zhou, W. Feng, R.-W. Zhang, L. Šmejkal, J. Sinova, Y. Mokrousov, and Y. Yao, Phys. Rev. Lett. **132**, 056701 (2024).

[18] X. Chen, S. Shi, G. Shi, X. Fan, C. Song, X. Zhou, H. Bai, L. Liao, Y. Zhou, H. Zhang, A. Li, Y. Chen, X. Han, S. Jiang, Z. Zhu, H. Wu, X. Wang, D. Xue, H. Yang, and F. Pan, Nat. Mater. **20**, 800 (2021).

[19] H. Bai, L. Han, X. Y. Feng, Y. J. Zhou, R. X. Su, Q. Wang, L. Y. Liao, W. X. Zhu, X. Z. Chen, F. Pan, X. L. Fan, and C. Song, Phys. Rev. Lett. **128**, 197202 (2022).

[20] S. Karube, T. Tanaka, D. Sugawara, N. Kadoguchi, M. Kohda, and J. Nitta, Phys. Rev. Lett. **129**, 137201 (2022).

[21] A. Bose, N. J. Schreiber, R. Jain, D.-F. Shao, H. P. Nair, J. Sun, X. S. Zhang, D. A. Muller, E. Y. Tsymbal, D. G. Schlom, and D. C. Ralph, Nat. Electron. **5**, 267 (2022).

[22] R. D. Gonzalez Betancourt, J. Zubáč, R. Gonzalez-Hernandez, K. Geishendorf, Z. Šobáň, G. Springholz, K. Olejník, L. Šmejkal, J. Sinova, T. Jungwirth, S. T. B. Goennenwein, A. Thomas, H. Reichlová, J. Železný, and D. Kriegner, Phys. Rev. Lett. **130**, 036702 (2023).

[23] H. Bai, Y. C. Zhang, Y. J. Zhou, P. Chen, C. H. Wan, L. Han, W. X. Zhu, S. X. Liang, Y. C. Su, X. F. Han, F. Pan, and C. Song, Phys. Rev. Lett. **130**, 216701 (2023).

[24] A. Hariki, T. Yamaguchi, D. Kriegner, K. W. Edmonds, P. Wadley, S. S. Dhesi, G. Springholz, L. Šmejkal, K. Výborný, T. Jungwirth, and J. Kuneš, arXiv:2305.03588.

[25] T. Aoyama and K. Ohgushi, arXiv:2305.14786.

[26] O. Fedchenko *et al.*, arXiv:2306.02170.

[27] C. F. Squire, Phys. Rev. **56**, 922 (1939).

[28] T. Komatsubara, M. Murakami, and E. Hirahara, J. Phys. Soc. Jpn. **18**, 356 (1963).

[29] W. Szuszkiewicz, B. Hennion, B. Witkowska, E. Łusakowska, and A. Mycielski, Phys. Status Solidi C **2**, 1141 (2005).

[30] J. B. Efrem D'Sa, P. A. Bhobe, K. R. Priolkar, A. Das, S. K. Paranjpe, R. B. Prabhu, and P. R. Sarode, J. Magn. Magn. Mater. **285**, 267 (2005).

[31] R. Juza, A. Rabenau, and G. Pascher, Z. Anorg. Allg. Chem. **285**, 61 (1956).

[32] D. Kriegner, H. Reichlova, J. Grenzer, W. Schmidt, E. Ressouche, J. Godinho, T. Wagner, S. Y. Martin, A. B. Shick, V. V. Volobuev, G. Springholz, V. Holý, J. Wunderlich, T. Jungwirth, and K. Výborný, Phys. Rev. B **96**, 214418 (2017).

[33] P. E. Faria Junior, K. A. de Mare, K. Zollner, K.-H. Ahn, S. I. Erlingsson, M. van Schilfgaarde, and K. Výborný, Phys. Rev. B **107**, L100417 (2023).

[34] M. Kitamura, S. Souma, A. Honma, D. Wakabayashi, H. Tanaka, A. Toyoshima, K. Amemiya, T. Kawakami, K. Sugawara, K. Nakayama, K. Yoshimatsu, H. Kumigashira, T. Sato, and K. Horiba, Rev. Sci. Instrum. **93**, 033906 (2022).

[35] G. Kresse and J. Furthmüller, Phys. Rev. B **54**, 11169 (1996).

[36] S. Li, J. Wu, B. Liang, L. Liu, W. Zhang, N. Wazir, J. Zhou, Y. Liu, Y. Nie, Y. Hao, P. Wang, L. Wang, Y. Shi, and S. Li, Chem. Mater. **34**, 873 (2022).

[37] J. Allen, G. Lucovsky, and J. Mikkelsen, Solid State Commun. **24**, 367 (1977).

[38] C. Ferrer-Roca, A. Segura, C. Reig, and V. Muñoz, Phys. Rev. B **61**, 13679 (2000).

[39] J. Wasscher, Ph.D. thesis, Technische Hogeschool Eindhoven, 1969.

[40] D. Kriegner, K. Výborný, K. Olejník, H. Reichlová, V. Novák, X. Marti, J. Gazquez, V. Saidl, P. Němec, V. V. Volobuev, G. Springholz, V. Holý, and T. Jungwirth, Nat. Commun. **7**, 11623 (2016).